Chinese Chemical Letters 37 (2026) 111397

Contents lists available at ScienceDirect

Chinese Chemical Letters

journal homepage: www.elsevier.com/locate/cclet

Insight into electrocatalytic nitrate reduction to ammonia on titanium oxide: Synergistic effects of crystalline phase and surface oxygen defects

Shuxian He[1], Fei Shen[1], Jiahong Zou, Peng Cheng, Wenyang Fu, Yan Zou, Ling Chen, Xiaoshu Lv*, Guangming Jiang*

Engineering Research Center for Waste Oil Recovery Technology and Equipment, Ministry of Education, Chongqing Technology and Business University, Chongqing 400067, China

ARTICLE INFO

Article history:
Received 17 December 2024
Revised 7 April 2025
Accepted 28 May 2025
Available online 29 May 2025

Keywords:
Nitrate reduction
TiO_2
Defects
Phase composition
Oxygen vacancy

ABSTRACT

While TiO_2 is a promising catalyst for electrocatalytic nitrate (NO_3^--N) reduction to NH_3 (ENRR), how the crystalline phase (anatase (A) or rutile (R)) and surface oxygen vacancy (O_v) synergize in ENRR remains ambiguous. Herein a series of nitrogen-doped TiO_2 catalysts with controlled phase composition and O_v number are prepared by calcinating titanium nitride powders in an air atmosphere at specific temperatures (N-TiO_2-*x*, *x* = 450–750 °C). Generally, higher temperatures lead to increased R-TiO_2 content but decreased O_v number. The ENRR performances of these N-TiO_2 are higher than that of pure A- and R-TiO_2, and vary in volcano-like trends against both the R-TiO_2 content and O_v number. Combined control experiments and theoretical simulation demonstrate that O_vs are the active sites for ENRR, but their functions differ between A-TiO_2 and R-TiO_2. Specifically, the O_vs on R-TiO_2 are more active in NO_3^- conversion and renew more easily during reaction, while those on A-TiO_2 perform better in proton adsorption. The synergy between O_vs on R-TiO_2 and A-TiO_2 promotes the ENRR on the phase-mixed N-TiO_2. Furthermore, as the catalyst varies from N-TiO_2–450 to -750, the overall efficacy of O_vs in proton transfer decreases due to the decreased number of O_vs on A-TiO_2, while the mean activity and renewability of them improve as a higher proportion of O_vs are distributed on R-TiO_2. The tug-of-war between the two opposing trends results in a peak ENRR performance on N-TiO_2–650 (mass activity: 22.2 $mg_N\ h^{-1}\ g_{cat.}^{-1}$; NH_3-N selectivity: 98.8%; Faradaic efficiency: 79.4%). These findings offer a deeper understanding of ENRR on TiO_2, and provide new insights for the design of efficient catalysts.

© 2025 Published by Elsevier B.V. on behalf of Chinese Chemical Society and Institute of Materia Medica, Chinese Academy of Medical Sciences.

Nitrate (NO_3^-) is an ubiquitous pollutant in environment, originating from the extensive use of nitrogenous fertilizers, inadequate discharge of nitrate-laden domestic/industrial wastewater, and NO_x deposition. It poses serious threats to ecosystems and human health (*e.g.*, the methemoglobinemia) [1]. Conventional physical-chemical treatments like ion exchange, electrodialysis and reverse osmosis can effectively separate NO_3^- but produce concentrated solutions that require post-treatment steps. Biological denitrification is time-consuming and significantly affected by surrounding conditions, such as dissolved oxygen and temperature [2]. Recently, electrochemical nitrate reduction (ENRR) has emerged as a highly competitive alternative owing to its mild reaction conditions and sustainability [3,4]. More intriguingly, when the product is ammonia (NH_3), the ENRR process utilizing nitrate pollutants as raw materials can be a promising alternative to the energy- and carbon-intensive Haber-Bosch process for NH_3 synthesis [5,6].

To accelerate the eight-electron reduction of NO_3^--N and improve NH_3 selectivity within ENRR, various catalysts have been developed, including transition metals (Pt, Pd, Cu, Co, Ti, Fe and their alloys) [7,8], oxides (CuO, CoO and TiO_2) [9–11] and single- or di-atomic catalysts [12,13]. Among them, TiO_2 has emerged as a preferred ENRR catalyst owing to its substantial chemical stability, abundance and high NH_3-N selectivity [14,15]. For instance, Jia *et al.* ever developed a TiO_2 nanotube-based powder catalyst that achieved a relatively high Faradaic efficiency (FE%) of 85.0% and a high NH_3 selectivity 87.1% in ENRR [16]. Ren *et al.* ever designed a series of oxygen vacancy (O_v)-bearing TiO_{2-x} nanoarray catalysts with anatase (A-TiO_2), rutile (R-TiO_2) and mixed-phase (A + R) crystal structures, respectively [17]. They demonstrated that

* Corresponding authors.
E-mail addresses: lyuxiaoshu@zju.edu.cn (X. Lv), jiangguangming@zju.edu.cn (G. Jiang).
[1] These two authors contributed equally to this work.

https://doi.org/10.1016/j.cclet.2025.111397
1001-8417/© 2025 Published by Elsevier B.V. on behalf of Chinese Chemical Society and Institute of Materia Medica, Chinese Academy of Medical Sciences.

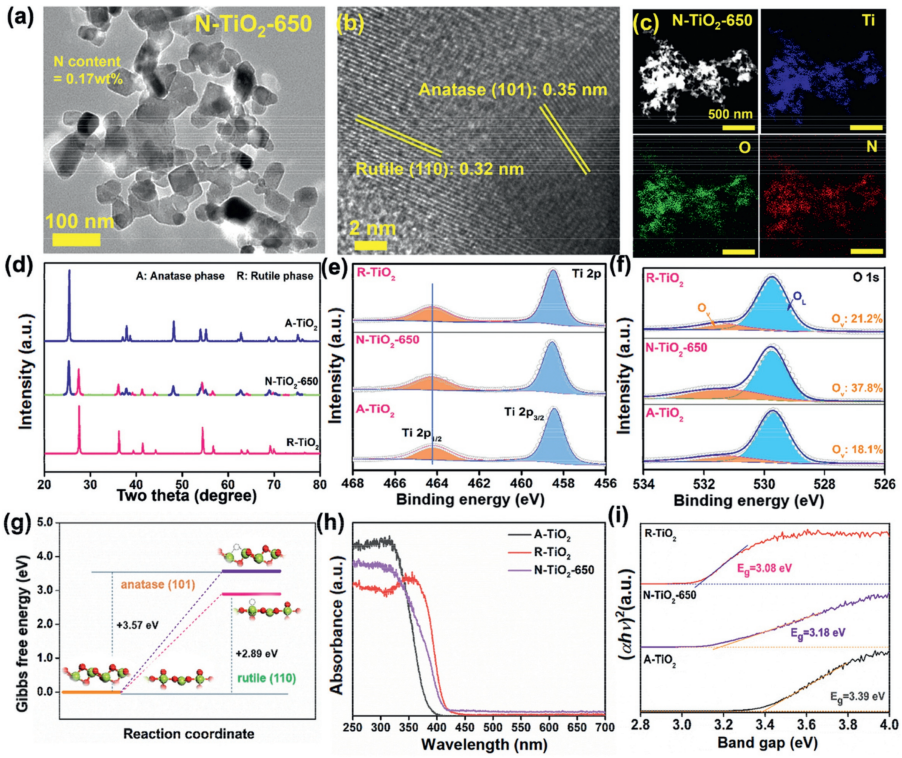


Fig. 1. As-synthesized N-TiO_2–650: (a) TEM images, (b) HRTEM image, and (c) EDS elemental mapping images. Comparison of N-TiO_2–650 with A-TiO_2 and R-TiO_2: (d) XRD patterns, (e) Ti 2p XPS spectra, (f) O 1s XPS spectra, (g) Gibbs free energies for the formation of O_v, (h) UV–vis-DRS patterns, and (i) band gaps.

the A-TiO_{2-x} afforded the highest NH_3 yield of 122 mg h^{-1} cm^{-2} and a FE% of 91.1%. Wei *et al.* developed a TiO_2 nanoparticle catalyst featuring a unique anatase-rutile heterojunction and O_vs, which enabled efficient ENRR with a FE% of 78.0% and NH_3 selectivity of 81.9% [18]. Zhang *et al.* also prepared a defective TiO_2 nanotube array catalyst on Ti mesh for ENRR, which delivered a high NH_3 selectivity of 91% and FE% of 85% [19]. Besides demonstrating robust ENRR efficiency under various reaction conditions, these studies reached a consensus that the O_vs on the TiO_2 surface were the active sites for ENRR [20,21]. They could capture and stabilize the N-intermediates by having their oxygen or nitrogen ends occupy the O_v site [22]. Along with strong adsorption, the N-O bonds of the N-intermediates were significantly activated, and their migration and inter-coupling over the catalyst surface were inhibited, resulting in a low energy barrier and high NH_3 selectivity for ENRR [16].

It is well documented that TiO_2 has two crystalline forms: A-TiO_2 and R-TiO_2, which generally coexist. Given that the surface structures of A-TiO_2 and R-TiO_2 differ, it can be inferred that the chemical structure of the O_v at their surfaces as well as their roles in ENRR should differ accordingly. Although some studies have explored the dependence of the ENRR on crystalline composition, the interplay between the crystalline phase and surface O_v in ENRR remains underexplored [18,23,24]. Herein we reported a facile approach to the defective and crystalline phase-mixed TiO_2 by calcinating the titanium nitride (TiN) powders under an air atmosphere [25]. Both the phase composition and surface O_v number within TiO_2 was controllable by tuning the calcination temperature (450–750 °C). The ENRR performances of these TiO_2 catalysts in terms of mass activity, NH_3-N selectivity, FE% and tolerance to impurities were then evaluated and compared to that of the commercially-available pure A-TiO_2 and R-TiO_2 phase, respectively. Finally, controlled experiments, *in-situ* spectrometric tests and theoretical calculations were combined to probe into the synergistic effects of the crystalline phase and O_v on ENRR [26].

The defective and phase-mixed TiO_2 with N doping (N-TiO_2) was prepared by calcining the TiN at an air atmosphere within a specific temperature range of 450–750 °C. The representative Transmission electron microscope (TEM) image of N-TiO_2 calcined at 650 °C (denoted as N-TiO_2–650) is presented in Fig. 1a, which shows irregular nanosheets with a mean lateral size of 20–30 nm. Corresponding High resolution transmission electron microscope (HRTEM) image in Fig. 1b reveals that the nanosheets display two distinct lattice fringes with the spacing of 0.350 and 0.322 nm, corresponding to the (101) plane of A-TiO_2 and the (110) plane of R-TiO_2. These results suggest the presence of a phase mixture in the N-TiO_2–650. The presence of N in N-TiO_2–650 is confirmed by solid elemental analysis, and its content is only 0.17 wt%. The Energy dispersive spectrometer (EDS) elemental mapping results in Fig. 1c reveal the uniform distribution of Ti, O and N on N-TiO_2–650. The XRD patterns of pure A-TiO_2, pure R-TiO_2 and N-TiO_2–650 in Fig. 1d demonstrate that the N-TiO_2–650 exhibits a mixed crystalline phase of rutile and anatase, which is in good agreement with the HRTEM results. The relative content of A-TiO_2 to R-TiO_2 is estimated to be 49.3/50.7 on basis of their peak intensity in the X-Ray diffraction (XRD) pattern. X-ray photoelectron spectroscopy (XPS) analyses on N-TiO_2–650, A-TiO_2 and R-TiO_2 are further conducted to investigate the electronic states of Ti and O in samples. The Ti 2p XPS spectra in Fig. 1e displays the Ti^{4+} species in three samples. No Ti^{3+} was detected possibly owing to its low content. The O 1s XPS spectra in Fig. 1f confirm the presence of O_v on the surface of all the three samples by the characteristic peak at 531.4 eV, corresponding to the Ti site that is coordination unsaturated. The surface O_v content can be estimated by the peak area ratio of O_v to ($O_L + O_v$) (O_L denotes lattice oxygen). The N-TiO_2–650 is indicated to have the largest number of O_v (37.8%), followed by R-TiO_2 (21.2%) and A-TiO_2 (18.1%). The high O_v content can be partially attributed to the unique preparation process of N-TiO_2 *via* TiN oxidation. Fig. 1g presents the Gibbs free energy for O_v generation on A-TiO_2 (101) and R-TiO_2 (110), which demonstrates that

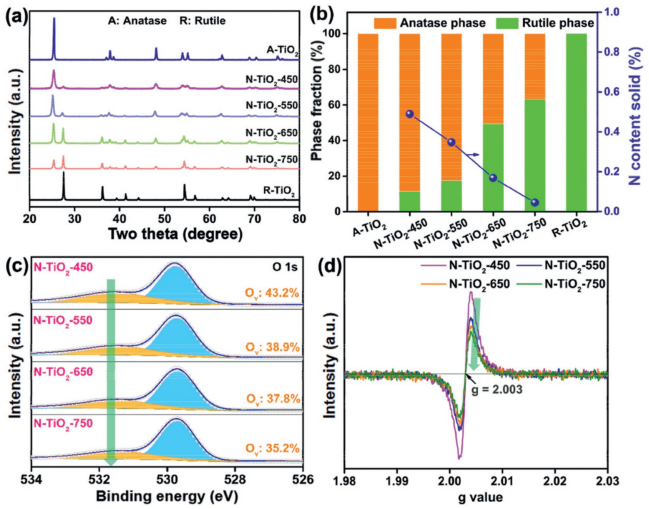


Fig. 2. The comparison of N-TiO_2 synthesized under different calcination temperatures: (a) XRD patterns, (b) the relative amount of A-TiO_2 to R-TiO_2 and the N content, (c) O 1s XPS spectra. and (d) EPR spectra.

the O_v is more easily formed on R-TiO_2 than on A-TiO_2 (2.89 *vs.* 3.57 eV). We can speculate from these results that more O_v distribute on R-TiO_2 surface in N-TiO_2. Fig. 1h shows the UV–vis-DRS spectra of three samples. The light absorption edge of N-TiO_2–650 is between those of A-TiO_2 and R-TiO_2. Correspondingly, the band gap increases from 3.08 eV of R-TiO_2, to 3.18 eV of N-TiO_2–650 and 3.39 eV of A-TiO_2 (Fig. 1i). These results confirm the presence of mixed phases in N-TiO_2–650.

The phase composition and the O_v number in N-TiO_2 can be controlled by tuning the calcination temperature. The XRD patterns in Fig. 2a show that the R-TiO_2 is gradually accumulated in N-TiO_2 along with the increase in calcination temperature. Fig. 2b summarizes the relative amount of A-TiO_2 to R-TiO_2 as well as the N content in N-TiO_2. As the calcination temperature increases, the proportion of R-TiO_2 rises, while the N content decreases from 0.49% to 0.05%. This occurs because the N atoms in TiN are gradually replaced by O atoms during the oxidation process. Generally, more complete oxidation at higher temperatures results in lower N contents. The UV–vis-DRS spectra in Fig. S1 (Supporting information) reveal that the band gaps of these N-TiO_2 follow a descending order of A-TiO_2 > N-TiO_2–450 > N-TiO_2–550 > N-TiO_2–650 > N-TiO_2–750 > R-TiO_2. Furthermore, N-TiO_2–450 and N-TiO_2–550 exhibit distinct absorption peaks in the visible light range of 450–500 nm, which can be attributed to the formation of intermediate energy levels induced by N doping. The O 1s XPS spectra in Fig. 2c show that as the temperature increases, the O_v content decreases from 43.2% to 35.2%. The same variation trend of the O_v content within this samples were observed in the EPR results present in Fig. 2d. This reduction in O_v number should be associated with the reduced N doping observed at higher calcination temperatures.

Fig. 3a exhibits the Linear sweep voltammetry (LSV) curves of the A-TiO_2, R-TiO_2 and N-TiO_2–650 in the presence and absence of NO_3^--N, respectively. In compared to A-TiO_2 and R-TiO_2, N-TiO_2–650 displays a smaller current response to hydrogen evolution in the absence of NO_3^--N while sharper current increase in the presence of NO_3^--N, implying a more effective ENRR on the phase-mixed N-TiO_2–650. The ENRR performances of A-TiO_2, R-TiO_2 and N-TiO_2–650 are further evaluated by potential-controlled batch tests at −0.80 V *vs.* RHE. Plotting the concentrations of NO_3^--N, NO_2^--N, NH_3-N and total N versus reaction time in Fig. 3b show that all the three catalysts are effective in converting NO_3^--N to NH_3-N with minimal residue of NO_2^--N at the end of reaction. Noted that the total nitrogen number in the solution remains almost constant among the three catalysts, indicating that minimal other products, such as N_2 and N_2O, are formed. As expected, N-TiO_2–650 affords the highest conversion efficiency of 91.8% within 6 h, followed by A-TiO_2 (72.9%) and R-TiO_2 (42.1%). To explore more about the phase-dependent ENRR activity of TiO_2, all the N-TiO_2-*x* (*x* = 450, 550, 650 and 750) are subjected to potential-controlled batch ENRR tests. Fig. 3c shows that the removal kinetics of NO_3^--N vary in a volcano-like trend with the *x* value. The N-TiO_2–650 delivers the fastest NO_3^- removal, followed by N-TiO_2–550, N-TiO_2–450 and N-TiO_2–750. The product distributions at the end of reaction are presented in Fig. 3d. As observed, the NO_3^- are almost completely converted to NH_3-N with minimal formation of NO_2^--N, resulting in the NH_3-N selectivity exceeding 98% for all the four samples. Fig. 3e summarizes the mass activities and FE% of A-TiO_2, R-TiO_2 and N-TiO_2-*x*. As observed, the N-TiO_2-*x* outperform both A-TiO_2 and R-TiO_2 in terms of mass activity and FE%. Among the N-TiO_2-x samples, N-TiO_2–650 affords both the highest mass activity (22.2 $mg_N\ h^{-1}\ g_{cat.}{}^{-1}$) and FE% (79.4%).

Given the high ENRR performance, N-TiO_2–650 is considered a promising catalyst for NH_3 synthesis using NO_3^--N pollutants as raw materials. Durability is a key descriptor of catalytic performance, and the durability of N-TiO_2–650 is evaluated through cycling batch ENRR experiments. The results in Fig. 3f show that the conversion efficiency of NO_3^--N to NH_3-N remains above 90% over 5 cycles, with the NO_2^--N yield staying below 0.5 mg/L. Accordingly, N-TiO_2–650 is expected to be durable in long-term ENRR. To evaluate the versatility of N-TiO_2–650 for various application scenarios, its ENRR performance is reassessed under different working potentials and in the presence of impurity ions and dissolved organics that coexists with NO_3^--N in wastewater. Fig. 4a depicts the time-course C/C_0 for NO_3^--N during ENRR on N-TiO_2–650 under different working potentials ranging from −0.60 V to −0.90 V. It is observed that ENRR does not begin until the potential is more negative than −0.70 V, with a more negative potential leading to accelerated NO_3^--N conversion. Fig. 4b shows that less NO_2^- remains and more NH_3-N is formed at more negative potentials, indicating increased NH_3-N selectivity under these conditions. It is noted that the N mass balance is not achieved and the FE% for ENRR decreases to 39.2% at −0.90 V, compared to 79.4% at −0.80 V. These phenomena may result from the predominance of HER at this negative potential, which carries some N species away from the solution while simultaneously wasting electrons. Fig. 4c exhibits the time-course C/C_0 for NO_3^--N during ENRR on N-TiO_2–650 under in the presence of Cl^- (5 mmol/L), CO_3^{2-} (1 mmol/L), Mg^{2+}(1 mmol/L), Ca^{2+} (2 mmol/L) and HA (3.3 mg/L). Their concentrations are set to approximate those in natural water body [3]. Fig. 4c shows that the impurities, with the exception of Cl^- and natural organic materials (NOMs), exert minimal effects on the ENRR kinetics. In the presence of 5 mmol/L Cl^- and 3.3 mg humic acid (representative of NOMs), the conversion efficiency at the end of reaction drops to 71.5% and 85.9%, respectively, compared to 91.3% in the control experiment. Fig. 4d demonstrate that except for humic acid, the other impurities show limited effects on the NH_3 selectivity. The negative effects of Cl^- and humic acid can be attributed to their potential to occupy active sites and alter the structure of the electric double layer at the electrode/solution interface [20,27]. These results demonstrate the high tolerance of N-TiO_2–650 to impurities, but further efforts are required to maintain its high performance under more complex conditions in wastewater.

To probe into the synergistic effects of phase composition and O_v on ENRR, *in-situ* test is first performed at the potentials of −0.70, −0.80 and −0.90 V, respectively, to identify the reaction pathway on N-TiO_2–650. $K^{15}NO_3$ is used as the source of nitrate to eliminate interference from the nitrogen reduction reaction for N-intermediate identification. The spectra in Fig. 5a demonstrate the occurrences of NO, N, N_2, NH, NH_2 and NH_3, while N_2O and

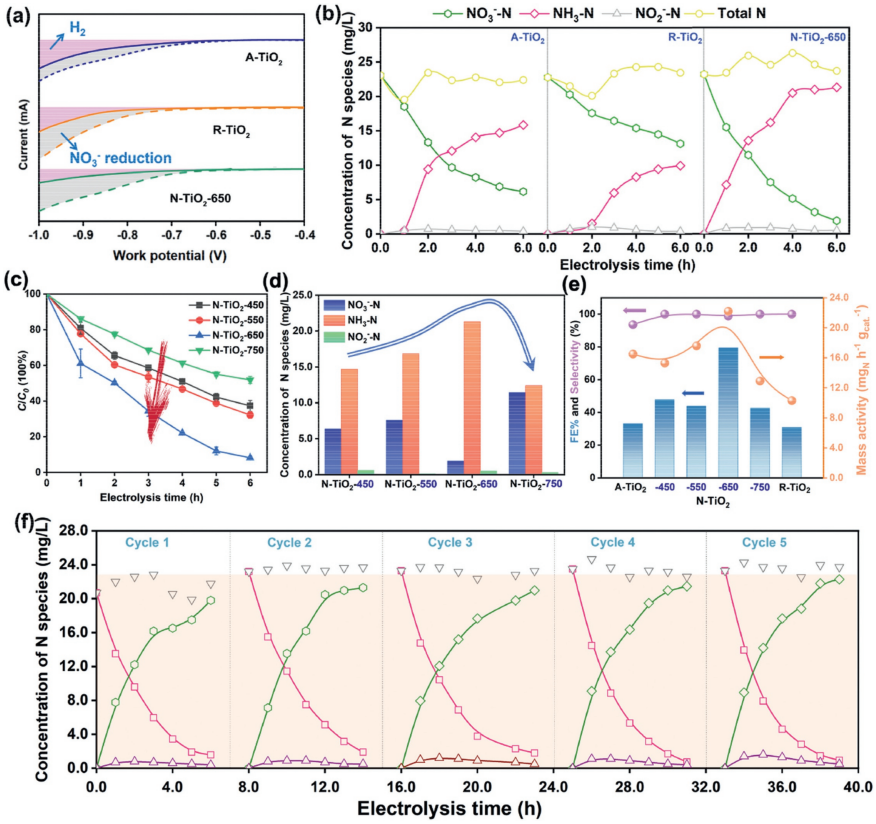


Fig. 3. (a) LSV curves for N-TiO_2–650, A-TiO_2 and R-TiO_2. (b) The product distribution for ENRR on N-TiO_2–650, A-TiO_2 and R-TiO_2, respectively. (c) The reaction time-course C/C_0, (d) product distribution at the end of reaction and (e) FE% and mass activity for N-TiO_2-*x*. (f) Cycled ENRR tests on N-TiO_2–650. Reaction conditions: −0.80 V in 50 mmol/L Ar-saturated Na_2SO_4 solution with a feeding NO_3^--N concentration of 22.5 mg/L.

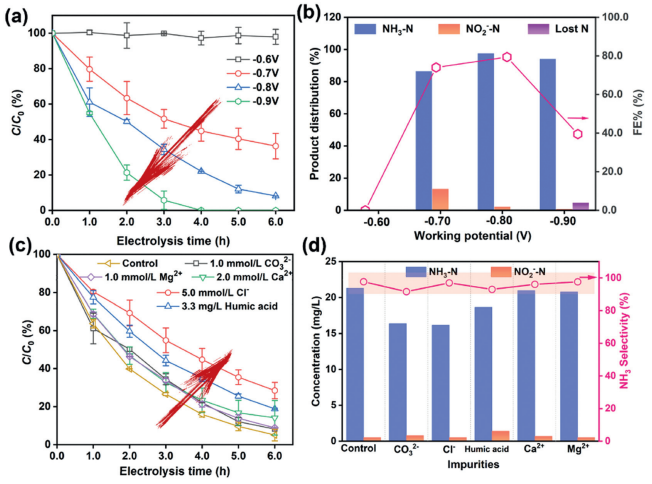


Fig. 4. (a) Time-course C/C_0 and (b) product distribution at the end of reaction under different working potentials. (c) Time-course C/C_0 and (d) product distribution at the end of reaction in the presence of impurity ions and NOMs.

NH_2OH are absent [12]. When coupling the results with the detected NO_2^- and NH_3 in solution, the ENRR is considered to proceed *via* the mass diffusion of NO_3^- from bulk solution to catalyst surface, forming adsorbed $^*NO_3$. Subsequently, the $^*NO_3$ evolves to $^*NO_2$, $^*NO$ and $^*N$ through stepwise dehydrogenation reactions, and $^*N$ further converts to $^*NH$, $^*NH_2$ and $^*NH_3$ through stepwise hydrogenation reactions (Fig. 5a) [28]. These spectra also suggest that the hydrogenation of $^*N$ predominates over the coupling of $^*N$-$^*N$ to N_2, consistent with the high NH_3 selectivity achieved by N-TiO_2–650 [29]. The resolution of strong peaks assigned to H_2 suggests that side hydrogen evolution is inevitable on N-TiO_2–650, resulting in an overall FE% below 100%. Furthermore, the signals for all the N-intermediates are stronger under more negative potentials, verifying the boosted ENRR at these conditions.

According to Singh *et al.*'s results, the adsorption strengths of N-intermediates on the catalyst can be described by the adsorption strength of a single N or O atom on the catalyst [30]. In this context, the adsorption strengths of the single O and N atom on pristine A-, R-TiO_2, as well as them with surface O_v sites were compared by Density functional theory (DFT) calculations, respectively [12,31]. The A-TiO_2 (110) and R-TiO_2 (101) facets are modeled separately for investigation, and the O_v site is created by removing one O atom from the facet. The results in Fig. 5b show that the adsorption strengths of the single N and O atom on the O_v sites of both TiO_2 phases are much larger than that on pristine surface. It is suggested that the O_v sites are more likely to be the active sites for ENRR, consistent with the results reported in literature [20]. Furthermore, compared to R-TiO_2 (110), the O_v site on A-TiO_2 (101) binds more strongly with N-intermediates, implying that the activity of the O_v site within ENRR differs between A-TiO_2 and R-TiO_2.

The thermodynamics for ENRR on the O_v sites of A-TiO_2 (101) and R-TiO_2 (110) were further investigated by DFT calculations to gain more insight to the role of O_v [32]. The Gibbs free energy profiles in Fig. 5c show that the overall ENRR process on the O_v sites of both A-TiO_2 (101) and R-TiO_2 (110) is thermodynamically spontaneous, owing to the negative value for $^*NO_3$ conversion to $^*NH_3$ [32]. On the O_v site of R-TiO_2 (110), only the dehydrogenation step of $^*NOH$ to $^*N$ requires additional energy input. In contrast, on the O_v site of A-TiO_2 (101), there are energy barriers for two steps: the dehydrogenation conversion of $^*NOH$ to $^*N$ and the hydrogenation conversion of $^*NH_2$ to $^*NH_3$. Additionally, the energy barrier for

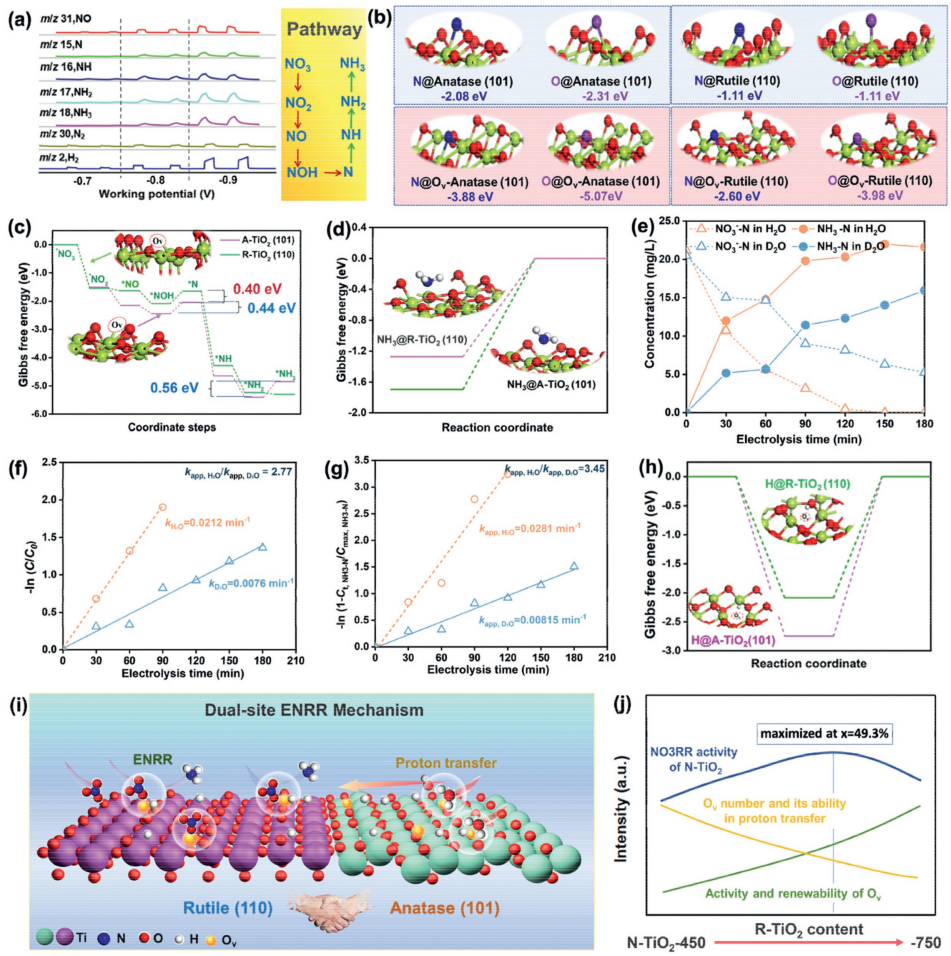


Fig. 5. (a) The DEMS spectra for the ENRR on N-TiO_2–650 using $K^{15}NO_3$ as nitrate source as well as the proposed reaction pathway. (b) The adsorption energy for single N and O atom on the pristine and defective A-TiO_2 (101) and R-TiO_2 (110), respectively. (c) Gibbs free energy diagrams for the conversion of $^*NO_3$ to $^*NH_3$ on the O_v site of A-TiO_2 (101) and R-TiO_2 (110), respectively. (d) Gibbs free energy for NH_3 desorption from the O_v site of A-TiO_2 (101) and R-TiO_2 (110). (e) Plotting of the concentration of NO_3^--N and NH_3-N against reaction time and (f, g) expression of the *pseudo*-first-order kinetics law for the NO_3^--N removal and NH_3-N production during ENRR on N-TiO_2–650 in the H_2O and D_2O media, respectively. (h) Gibbs free energy diagram for hydrogen adsorption on the O_v site of A-TiO_2 (101) and R-TiO_2 (110), respectively. (i) Proposed dual-site mechanism for ENRR within the phase-mixed N-TiO_2. (j) Schematic illustration in the relationship between the ENRR performance and content of Rutile in N-TiO_2.

ENRR on the O_v site of R-TiO_2 (110) (0.40 eV) is smaller than that on the O_v site of A-TiO_2 (101) (0.44 and 0.56 eV), demonstrating that the O_v on R-TiO_2 is more active for NO_3^- conversion. Besides reactivity, the renewability of the O_v site, associated with the desorption kinetics of NH_3 from it, is critical for maintaining its activity [33]. Herein the energy barriers for NH_3 desorption from the O_v sites of A-TiO_2 and R-TiO_2 are investigated by DFT calculations [34]. The Gibbs energy profiles in Fig. 5d reveal that NH_3 desorption is thermodynamically unfavorable on both TiO_2 phases due to the strong affinity of the O_v sites with NH_3. Nevertheless, there is a lower energy barrier for NH_3 desorption from the R-TiO_2 (110), indicating that the O_v site on R-TiO_2 can be more easily renewed compared to that on A-TiO_2 [35].

Protons are essential reactants for ENRR, and the kinetics of their transfer from H_2O molecules to reactants on catalyst surface are closely associated with the denitrification kinetics [7,36]. To assess the efficacy of proton transfer kinetics, kinetic isotope experiments (KIE) are performed for ENRR on N-TiO_2–650. A KIE value obtained within these experiments serves as a key descriptor of the proton transfer kinetics from H_2O dissociation. It is defined as the ratio of NO_3^- removal kinetics or NH_3 production kinetics in H_2O versus D_2O media, respectively [37]. Fig. 5e plots the concentrations of NO_3^--N and NH_3-N against the electrolysis time in the two media, respectively. Compared to H_2O media, both NO_3^- removal and NH_3 production become much slower in D_2O media. Figs. 5f and g demonstrate that both NO_3^- removal and NH_3 production follow pseudo-first-order kinetics, with the KIE value calculated as $k_{app,H_2O}/k_{app,D_2O}$ reaching 2.77 for NO_3^- removal and 3.45 for NH_3 production (k_{app} refers to apparent reaction rate constant). These results demonstrate that the ENRR on N-TiO_2 largely depends on the proton transfer kinetics [38]. To compare the capability of O_v sites on A-TiO_2 and R-TiO_2 in proton adsorption, the Gibbs free energy profiles for proton adsorption on these O_v sites were investigated by DFT calculations. Fig. 5h exhibits that the H adsorption is spontaneous on the O_v site of both A- and R-TiO_2, owing to the negative value of ΔG [39]. Furthermore, the O_v site on the A-TiO_2 surface has a greater affinity for protons than that on R-TiO_2. This suggests that the defective A-TiO_2 is more active in proton transfer, making ENRR less dependent on proton transfer.

From the above, we can conclude that the O_vs on the TiO_2 surface are the active sites for ENRR, but their roles differ between A-TiO_2 and R-TiO_2. Specifically, the O_vs on the R-TiO_2 surface are more active for ENRR and renew more easily during ENRR, while those on A-TiO_2 surface perform better in proton adsorption. Accordingly, a dual-site mechanism involving the O_v site on R-TiO_2 surface and the O_v site on A-TiO_2 surface can be expected on the defective and phase-mixed N-TiO_2, with the synergy of the dual O_v sites contributing to significantly enhanced ENRR performance

(Fig. 5i) [40]. Based on the distinct functions of the O_vs on R-TiO_2 and A-TiO_2 surfaces, it also becomes clear why the ENRR efficiency shows a volcano-like variation with the catalyst varying from N-TiO_2–450 to N-TiO_2–750. As schematically described in Fig. 5j, as the catalyst varies from N-TiO_2–450 to N-TiO_2–750, the content of R-TiO_2 in the catalyst rises while the O_v number decreases. Correspondingly, the overall efficacy of O_v in proton transfer decreases owing to the decreased number of O_vs distributed on the A-TiO_2 surface. Nevertheless, the mean activity and renewability of them improve as an increased proportion of O_vs are distributed on the R-TiO_2 surface. The tug-of war of the two reverse varying trends leads to a peak ENRR efficiency on N-TiO_2–650 with a moderate R-TiO_2 content of 49.3%.

Herein the synergy between phase composition and O_v on TiO_2 for ENRR is investigated using phase-mixed and defective N-TiO_2 as platform catalysts. The N-TiO_2 are prepared by calcining TiN powders in an air atmosphere with the phase composition and O_v number controlled by calcination temperature. The ENRR performance of these N-TiO_2 samples surpasses that of pure A- and R-TiO_2, showing a volcano-like trend with respect to R-TiO_2 content and O_v number in the catalyst. Mechanistic studies reveal that O_vs are the active sites, but their functions differ between A-TiO_2 and R-TiO_2. Specifically, the O_vs on R-TiO_2 are more active in NO_3^- conversion and renew more easily during reaction, while those on A-TiO_2 are more efficient in proton adsorption. The synergy between O_vs on R-TiO_2 and A-TiO_2 leads to higher ENRR efficacy on N-TiO_2. On the other hand, when the catalyst varies from N-TiO_2–450 to −750, the overall efficacy of O_vs in proton transfer decreases owing to the decreased proportion of O_vs distributed on A-TiO_2. Nevertheless, the mean activity and renewability of O_vs improve as an increased proportion of them are distributed on R-TiO_2. The tug-of-war between the two opposing trends leads to a peak ENRR performance on N-TiO_2–650 with a moderate R-TiO_2 content of 49.3%. This work highlights the synergy between crystalline phase and surface defects in heterogeneous catalysis, suggesting that optimizing phase composition and enriching surface defects could enhance the ENRR on TiO_2.

Declaration of competing interest

The authors declare that they have no known competing financial interests or personal relationships that could have appeared to influence the work reported in this paper.

CRediT authorship contribution statement

Shuxian He: Writing – original draft, Investigation, Formal analysis. **Fei Shen:** Formal analysis, Data curation, Conceptualization. **Jiahong Zou:** Supervision, Software, Resources. **Peng Cheng:** Validation, Investigation. **Wenyang Fu:** Visualization, Validation. **Yan Zou:** Software, Resources, Project administration. **Ling Chen:** Visualization, Project administration. **Xiaoshu Lv:** Writing – review & editing, Investigation, Funding acquisition. **Guangming Jiang:** Writing – review & editing, Funding acquisition, Conceptualization.

Acknowledgments

The authors acknowledge the financial support by National Natural Science Foundation of China (Nos. 51978110 and 22176019), the Natural Science Foundation of Chongqing Science & Technology Commission (Nos. CSTB2023NSCQ-LZX0020 and CSTB2023NSCQ-BHX0207).

Supplementary materials

Supplementary material associated with this article can be found, in the online version, at doi:10.1016/j.cclet.2025.111397.

References

[1] L.L. Min, M.Y. Liu, L. Wu, et al., Environ. Sci. Technol. 56 (2022) 8–9.
[2] Y.G. Guo, X.Y. Cai, S.Y. Shen, G.F. Wang, J.L. Zhang, J. Catal. 402 (2021) 1–9.
[3] Z.X. Liu, F. Shen, L. Shi, et al., Environ. Sci. Technol. 57 (2023) 10117–10126.
[4] P. Gayen, J. Spataro, S. Avasarala, et al., Environ. Sci. Technol. 52 (2018) 9370–9379.
[5] B. Zhou, L.H. Yu, W.X. Zhang, et al., Angew. Chem. Int. Ed. 63 (2024) e202406046.
[6] Z.X. Wang, S.D. Young, B.R. Goldsmith, N. Singh, J. Catal. 395 (2021) 143–154.
[7] T. Xie, X. He, L. He, et al., Chin. Chem. Lett. 35 (2024) 110005.
[8] G.M. Jiang, Z.X. Liu, S.X. He, et al., ACS ES&T Eng. 4 (2024) 2912–2922.
[9] Y. Chen, X.Y. Xia, L. Tian, et al., Chin. Chem. Lett. 35 (2024) 109789.
[10] Y.F. Nie, H.P. Yan, S.W. Lu, et al., Chin. J. Catal. 59 (2024) 293–302.
[11] S.W. Lu, G.T. Lin, H.P. Yan, et al., ACS Catal. 14 (2024) 14887–14894.
[12] L. Shi, Y.M. Li, S.X. He, et al., Chem. Eng. J. 495 (2024) 153427.
[13] E. Murphy, Y.C. Liu, I. Matanovic, et al., Nat. Commun. 14 (2023) 4554–4568.
[14] Q.N. Song, S. Zhang, X.S. Hou, et al., J. Hazard. Mater. 438 (2022) 129455.
[15] W.P. Utomo, H. Wu, Y.H. Ng, Small 18 (2022) e2200996.
[16] R.R. Jia, Y.T. Wang, C.H. Wang, et al., ACS Catal. 10 (2020) 3533–3540.
[17] Z.F. Ren, Q.Y. Chen, X.G. An, et al., Inorg. Chem. 61 (2022) 12895–12902.
[18] Z. Wei, X.W. Niu, H.B. Yin, S.X. Yu, J.H. Li, Appl. Catal. A Gen. 636 (2022) 118596.
[19] Q. Zhang, Y.F. Li, M.N. Geng, et al., Appl. Catal. B: Environ. 330 (2023) 122658.
[20] M.E. Tang, Q.W. Tong, Y.M. Li, et al., Chin. Chem. Lett. 34 (2023) 108410.
[21] H.T. Du, H.R. Guo, K.K. Wang, et al., Angew. Chem. Int. Ed. 135 (2023) e202215782.
[22] J.W. Lin, X.Y. Lin, S.W. Lu, et al., Chem. Eng. Sci. 300 (2024) 120664.
[23] W.R. Liao, L. Qi, Y.L. Wang, et al., Adv. Funct. Mater. 31 (2021) 2009151.
[24] D. Liu, H.P. Yan, J.W. Lin, et al., Chem. Eng. Sci. 283 (2024) 119448.
[25] G.M. Jiang, J.W. Cao, M. Chen, X.M. Zhang, F. Dong, Appl. Surf. Sci. 458 (2018) 77–85.
[26] G.M. Jiang, M. Peng, L. Hu, et al., Chem. Eng. J. 435 (2022) 134853.
[27] D.M. Miller, M.J. Liu, K. Abels, et al., Energy Environ. Sci. 17 (2024) 5691–5705.
[28] H.B. Yin, F. Dong, Y.L. Wang, et al., Nano Lett. 23 (2023) 11899–11906.
[29] Y. Chen, T.P. Senftle, J. Catal. 438 (2024) 115706.
[30] J.X. Liu, D. Richards, N. Singh, B.R. Goldsmith, ACS Catal. 9 (2019) 7052–7064.
[31] L.M. Wu, J.Q. Feng, L.B. Zhang, et al., Angew. Chem. Int. Ed. 62 (2023) e202307952.
[32] W.R. Liao, J. Wang, G.H. Ni, et al., Nat. Commun. 15 (2024) 1264–1275.
[33] Y. Liu, X. Zhong, M.T. Liu, et al., Appl. Catal. B: Environ. Energy 355 (2024) 124205.
[34] L.H. Zhang, Y.T. Jia, J.Y. Zhan, et al., Angew. Chem. Int. Ed. 62 (2023) e202303483.
[35] Y. Li, J.X. Ma, T.D. Waite, M.R. Hoffmann, Z.W. Wang, Environ. Sci. Technol. 55 (2021) 10695–10703.
[36] X.X. Zhang, X.K. Liu, Z.F. Huang, et al., Energy Environ. Sci. 17 (2024) 6717–6727.
[37] W.X. Zhang, Y.C. Yao, Z.Y. Chen, et al., Environ. Sci. Technol. 58 (2024) 7208–7216.
[38] Y.F. Li, L.S. Li, S.L. Xu, et al., Angew. Chem. Int. Ed. 63 (2024) e202407810.
[39] Z.C. Wang, S.S. Liu, M.F. Wang, et al., ACS Catal. 13 (2023) 9125–9135.
[40] Y. Wang, S. Shu, M. Peng, et al., Nanoscale 13 (2021) 17504–17511.